



Cite this: *Phys. Chem. Chem. Phys.*,
2018, 20, 21151

In-plane thermal transport in black phosphorene/graphene layered heterostructures: a molecular dynamics study

Ting Liang, Ping Zhang, Peng Yuan and Siping Zhai

Heterostructures, which stack two different two-dimensional (2D) materials vertically together, have recently attracted tremendous attention. However, as one of their members, the in-plane thermal conductivity of black phosphorene/graphene (BP/GE) heterostructures, which plays a key role in determining their functional properties, is still unknown. In this work, we use non-equilibrium molecular dynamics (NEMD) simulations to study the in-plane thermal conductivities of BP/GE heterostructures and BP in BP/GE heterostructures. The effect on in-plane thermal conductivity with respect to the size effect (sample length), coupling strength, and hydrogen coverage is systematically examined. It is found that the in-plane thermal conductivity of infinite-size BP/GE bilayer heterostructures exhibits strong anisotropy, which is calculated to be 206.61 ± 6.35 (along the zigzag direction) and $51.02 \pm 3.72 \text{ W m}^{-1} \text{ K}^{-1}$ (along the armchair direction). In addition, we found that the enhancement of the coupling strength increases the in-plane thermal conductivity of BP/GE heterostructures and BP in BP/GE heterostructures, which may be due to an increase in phonon group velocities in BP and a stronger phonon coupling between BP and GE. In our research, hydrogenation has also been found to enhance the thermal conductivity of BP in heterostructures. The present study is expected to provide guidance for the study of the in-plane thermal transport properties in other 2D heterostructures, and it is of significance for understanding the thermal transport behavior of BP/GE heterostructures and BP in heterostructures and promoting their future applications in thermal management and thermoelectric devices.

Received 3rd May 2018,
Accepted 23rd July 2018

DOI: 10.1039/c8cp02831a

rsc.li/pccp

1. Introduction

Two-dimensional (2D) materials, such as graphene (GE), transition metal dichalcogenide (TMD), hexagonal boron nitride (BN), silicene, etc., have attracted extensive research interest in recent years due to their intriguing mechanical^{1,2} and superior electronic³ and thermal^{4,5} properties that can be applied to many different fields.^{6,7} In parallel to the efforts on searching and studying 2D materials, another research field has recently emerged that has attracted much attention. It involves stacking two different two-dimensional materials together vertically to form a novel material, named a heterostructure, with the 2D materials interacting with each other *via* weak van der Waals forces.⁸ By combining the two materials artificially, heterostructures can produce many excellent properties, which have been demonstrated in the form of rectifiers or solar cells,^{9,10} chemical sensors, and varied barrier electronic devices.¹¹ Recently, heterostructures have been used to tune the various

properties of two-dimensional materials, such as the bandgap of molybdenum disulfide,¹² Schottky barrier,^{13,14} and thermal conductivity.¹⁵ Therefore, fascinating heterostructures have been well studied both theoretically and practically, such as silicene/graphene,¹⁶ graphene/MoS₂^{17,18} and graphene/black phosphorene.¹⁹

Black phosphorene (BP), as a recent rising star of 2D materials,²⁰ exhibits a distinctive wrinkled structure with a high hole mobility of up to $1000 \text{ cm}^2 \text{ V}^{-1} \text{ s}^{-1}$,²¹ tunable band structures,¹⁴ and anisotropic thermal properties,²² thus leading to encouraging prospects for device applications. However, with the high integration of nanoelectronic devices, solving the heat dissipation issue has become the focus of attention.^{23,24} Pei and Zhang¹⁵ found that BP/GE heterostructures can increase the in-plane thermal conductivity of black phosphorene, with a net increase of 20–60%. With this motivation, we investigated BP/GE heterostructures and found that the in-plane thermal transport for the BP/GE heterostructures, based on molecular dynamics (MD) simulations, is still lacking. When BP and GE are combined to form hybrid heterostructures, their total in-plane thermal conductivity is yet to be determined. In addition, the influence of various factors on the thermal conductivity of BP in heterostructures remains unexplored.

School of Mechanical and Electrical Engineering, Guilin University of Electronic Technology, No. 1 Jinji Road, Guilin, Guangxi 541004, China.
E-mail: zp3631@gmail.com

Therefore, this work aims to study the in-plane thermal transport of BP/GE heterostructures *via* NEMD simulations. The in-plane thermal conductivity of bilayer structure heterostructures and BP in heterostructures will be calculated. The effects of the interface coupling strength and hydrogenation will be investigated and understood by the phonon density of states (PDOS) in the frequency domain.

2. Modeling and methodology

To model the BP/GE heterostructures, a supercell composed of a BP sheet with 6×11 unit cells is chosen, while the GE supercell is composed of 8×12 unit cells (both along the zigzag direction and armchair direction, respectively). Based on the BP and GE supercells, we stacked along the direction of the armchair of graphene and the zigzag edge of black phosphorene and constructed a $19.73 \text{ nm} \times 20.39 \text{ nm}$ heterostructure, as shown in Fig. 1(a-c). Thus, there are small mismatches between BP and GE in the x and y directions (both less than 1%). These comparable lattice mismatches between BP and GE are confirmed by recent first-principles calculations.^{14,19,25} Inspired by calculations of the thermal properties of other heterostructures,^{16,20} the lattice mismatches considered in our study have negligible effects on the thermal properties of the BP/GE heterostructures. Previous studies have shown that the thermal conductivity of phosphorene along the zigzag direction is greater than that along the armchair direction,^{26,27} while the in-plane thermal conductivity of graphene is isotropic.²⁸ Accordingly, we set the zigzag direction of black phosphorus as the x direction, with the armchair direction of black phosphorus as the y direction of the BP/GE heterostructures. Fig. 1 shows the atomistic configuration of simulation models: (a) single-layer BP, (b) BP/GE bilayer heterostructures, and (d) hydrogenated BP/GE heterostructures. Bilayer heterostructures are used to calculate the total thermal conductivity and thermal conductivity of black phosphorene in heterostructures.

All the MD simulations are performed using the large-scale atomic/molecular massively parallel simulator (LAMMPS) package.²⁹ Periodic boundary conditions are applied in the

two in-plane directions, with the free boundary condition along the out-of-plane z -direction to allow the interlayer distance to be adjusted freely. The interactions of the carbon atoms in graphene are described by the AIREBO potential,³⁰ while the Stillinger–Weber (SW) potential³¹ is employed to describe the covalent interaction between phosphorous atoms. To build a weak van der Waals force between BP and GE, the Lennard-Jones (LJ) potential is adopted as:

$$V(r) = 4\chi\varepsilon \left[\left(\frac{\sigma}{r} \right)^{12} - \left(\frac{\sigma}{r} \right)^6 \right], \quad (1)$$

where r is the distance between two atoms; ε and σ are the energy and distance constants, respectively. The cutoff distance of the LJ potential is set as 1.2 nm. The parameter χ is used to adjust the coupling strength between BP and GE. The LJ parameters are listed in Table 1, which are calculated using a universal force field (UFF) model.³²

In-plane thermal conductivities are calculated using NEMD simulations, which use the velocity-Verlet integration scheme³³ with a time step of 0.5 fs. To produce a stable temperature difference, we use the method of Jund and Jullien³⁴ to generate a non-equilibrium heat current. The simulation system is divided into 40 blocks along the transport direction, with block 1 chosen as a heat source and block 21 as a heat sink, as schematically shown in Fig. 2. During the simulation, the whole system is first equilibrated at $T = 300 \text{ K}$ under a constant volume and temperature ensemble (*NVT*) for 0.25 ns, and then the system is switched to an *NVE* ensemble and the heat source/sink heated/cooled with a given power Q for 1 ns. The given power Q is injected into the BP/GE heterostructures by performing a speed transformation for each particle according to:

$$\nu_i' = \nu_c + \alpha(\nu_i - \nu_c), \quad (2)$$

Table 1 LJ potential parameters used in MD simulations

Atom 1	Atom 2	Energy constant ε (meV)	Distance constant σ (Å)
C	P	7.76	3.563
P	H	5.02	3.133

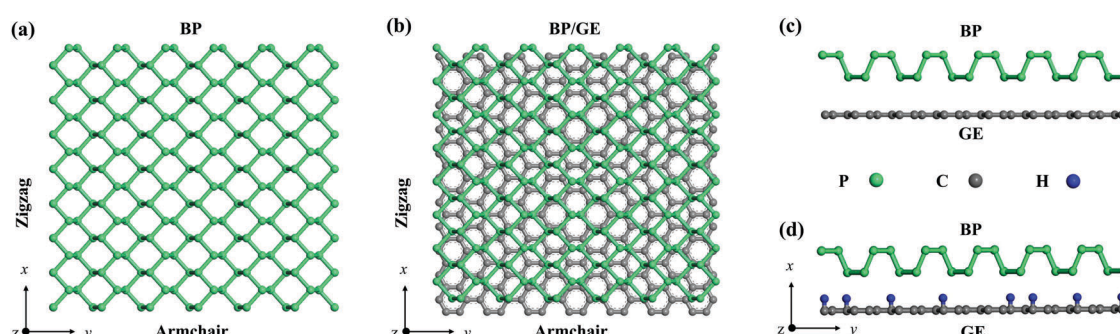


Fig. 1 The schematic models of single-layer BP and BP/GE heterostructures and hydrogenated BP/GE heterostructures. (a) Atomic structure of a single-layer BP, atomic structure of a BP/GE heterostructure: (b) top view and (c) side view, and (d) atomic structure of hydrogenated BP/GE heterostructures, which are formed by a random combination of H and C atoms.

where v_i' and v_i are the current and initial velocities of the thermostat atoms, respectively. v_c is the velocity of the center of mass, and α is the rescaling factor, which is given as follows:

$$\alpha = \sqrt{1 \pm \frac{\Delta\epsilon}{E_k^r}}, \quad (3)$$

where $\Delta\epsilon$ is the subtracted/injected energy from specified atoms and E_k^r is the relative kinetic energy

$$E_k^r = \frac{1}{2} \sum_i m_i v_i^2 - \frac{1}{2} \sum_i m_i v_c^2, \quad (4)$$

and the given power $Q = \Delta\epsilon/(\Delta t)$. Based on a constant heat flow of 1 ns, the system reaches a steady state and we can start to record the block temperatures and heat flux for another 1 ns. After obtaining the time-averaged temperature gradient $|\Delta T|$, the in-plane thermal conductivity of the steady system can be calculated according to Fourier's law as

$$k(\text{in}) = \frac{Q/2}{S|\Delta T|}, \quad (5)$$

where S is the cross-sectional area of the simulation system in the direction perpendicular to the heat current. In our calculation of S , the thickness of the BP/GE bilayer heterostructures is taken as $t_B = t_{\text{BP}} + t_{\text{GE}}$, where $t_{\text{BP}} = 5.24$ and $t_{\text{GE}} = 3.4 \text{ \AA}$ are the thicknesses of the BP and GE, respectively. Since the heat flows from the source to the sink in two opposite directions, the non-equilibrium heat current here should be taken as $Q/2$ (see Fig. 2).

The PDOS is computed from the Fourier transform³⁵ of the velocity autocorrelation function (VACF) of all the atoms as:

$$P(\omega) = \frac{1}{\sqrt{2\pi}} \int_0^\tau e^{i\omega t} \langle v(t)v(0) \rangle dt, \quad (6)$$

where $P(\omega)$ is the total PDOS at frequency ω . Since the VACF is normalized and dimensionless, the unit of PDOS is THz⁻¹. The ensemble average in eqn (6) is realized by time averaging over a period of 30 ps, with the sample velocities extracted from the simulation every 10 fs. The phonon power spectrum analysis provides a quantitative means to assess the power carried by phonons in a system. To quantitatively determine the overlap

of the two phonon power spectra, the overlap area factor S is defined as:

$$S = 2 \int_0^\infty \min\{P_{\text{BP}}(\omega), P_{\text{GE}}(\omega)\} d\omega, \quad (7)$$

where P_{BP} and P_{GE} are the two PDOS of black phosphorene and graphene, respectively.

3. Results and discussion

3.1 In-plane thermal conductivity of the BP/GE heterostructures

3.1.1 Anisotropy and size effect. Since the in-plane thermal conductivity of monolayer black phosphorene is anisotropic, with an anisotropy ratio ranging from 2.2 to 5.5,^{22,27} we consider whether the in-plane thermal conductivity of the BP/GE heterostructures is also anisotropic. Thus, we first performed MD simulations to study the anisotropy and effects of sample size on the in-plane thermal conductivity. Taking the $19.73 \times 20.39 (\text{x} \times \text{y}) \text{ nm}^2$ BP/GE bilayer heterostructures as an example, different given powers Q along the armchair direction and zigzag direction are added to the heat bath at each time step. After reaching the steady state, we obtained the temperature distribution along the heat flux direction, as shown in Fig. 3. Linear fitting is applied to the temperature profiles, to obtain an accurate temperature difference. Each simulation system performs three independent calculations by changing the random number, with standard error of the independent results reported in this paper. The in-plane thermal conductivities calculated using eqn (5) are 13.60 ± 0.37 and $8.02 \pm 0.34 \text{ W m}^{-1} \text{ K}^{-1}$ for the zigzag direction and armchair direction, respectively. Our results clearly show that the in-plane thermal conductivity of the BP/GE bilayer heterostructures also shows strong anisotropy, with a ratio of approximately 1.7.

To validate the simulation results, the in-plane thermal conductivity of a single-layer BP along the zigzag direction and armchair direction is calculated to be 5.40 ± 0.33 and $2.37 \pm 0.15 \text{ W m}^{-1} \text{ K}^{-1}$, respectively. The results agree well with previous reported values of approximately 5.57 and $2.32 \text{ W m}^{-1} \text{ K}^{-1}$ for almost the same in-plane dimensions and potential function.³¹ A calculation of the in-plane thermal conductivity along the

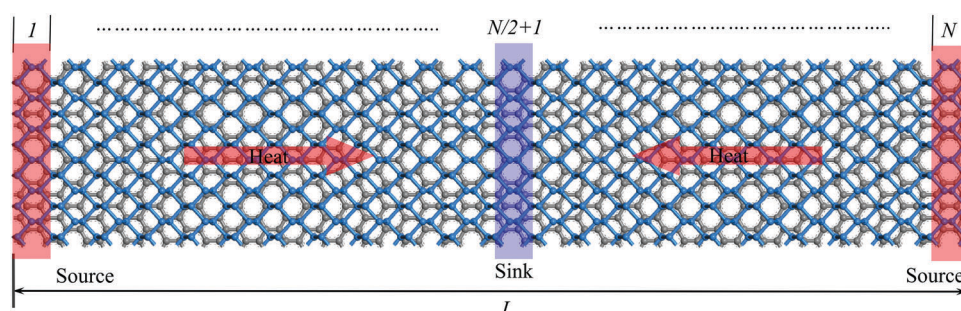


Fig. 2 A schematic picture for the heat flux setting. Here, the BP/GE heterostructure model along the length direction (L) is divided into $N = 40$ blocks, with block 1 acting as a heat source where energy flows in, while block $N/2 + 1 = 21$ acts as a heat sink where the energy flows out. Since periodic boundary conditions are applied in both planar directions, the heat flows from the source to the sink in two opposite directions.

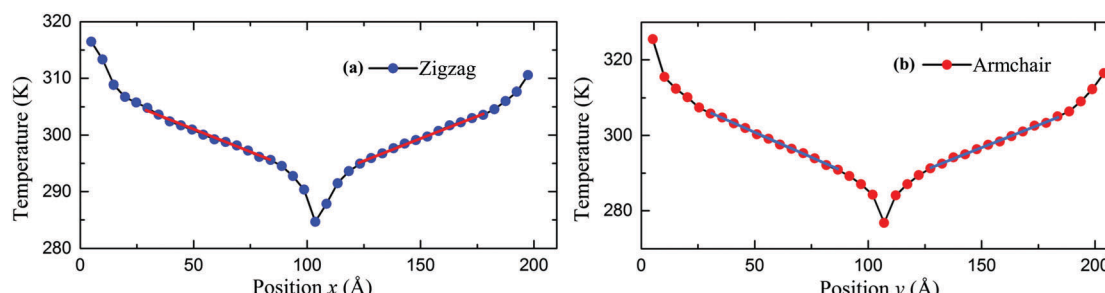


Fig. 3 The typical NEMD simulations temperature profiles obtained for (a) BP/GE bilayer heterostructures along the zigzag direction and (b) armchair direction. Linear fitting is applied in both temperature profiles.

zigzag direction and armchair direction of the BP layer in the BP/GE bilayer gives values of 12.92 ± 0.36 and 5.86 ± 0.29 W m $^{-1}$ K $^{-1}$, respectively, which are much higher compared to the isolated BP monolayer. In a previous study,¹⁵ the in-plane thermal conductivity of the BP layer in the BP/GE heterostructures was found to have a net growth of 20–60% due to the enhanced group velocities and extremely strong phonon coupling. Meanwhile, for the GE layer in the BP/GE bilayer, the obtained thermal conductivity of 87.43 ± 1.06 W m $^{-1}$ K $^{-1}$ is close to that reported for isolated GE monolayers with similar sizes by using the second-generation AIREBO potential.^{30,36,37} In addition, by using the Tersoff potential³⁸ with optimized parameters³⁹ for graphene, the thermal conductivity of the GE layer in BP/GE is calculated to be 84.58 ± 1.52 W m $^{-1}$ K $^{-1}$, which shows little difference from the value calculated above. The phenomenon of no increase in the thermal conductivity of the GE in bilayer heterostructures is also found in another study¹⁸ of the thermal transport in a graphene–MoS₂ bilayer heterostructure.

Experimentally, the size of the synthetic heterostructures ranges from tens of nanometers to several microns.^{40,41} Since the size of a two-dimensional material is very important for determining the phonon transport mechanism (diffusion or ballistic transport), it is necessary to study the system size effect for the BP/GE bilayer heterostructures. Moreover, the in-plane thermal conductivity is affected by the system size, while the

phonon mean free path (λ) is larger than the length (L) of the system. Actually, when $L < \lambda$, phonon conduction is called ballistic heat transfer and phonon scattering is suppressed; thus, the thermal conductivity increases with an increase in system size. The phonon mean free path of graphene is measured to be ~ 775 nm at near room temperature, which is much larger than the size of graphene in a BP/GE bilayer heterostructure. To extrapolate the conductivity values of finite BP/GE heterostructure systems to the limit of infinite length, an inverse fitting procedure is employed. The extrapolation formula is the one proposed by Schelling *et al.*⁴²

$$\frac{1}{k(L)} = \frac{1}{k_\infty} \left(1 + \frac{\lambda}{L} \right), \quad (8)$$

where k_∞ is the intrinsic thermal conductivity of an infinite length system ($L \rightarrow \infty$).

In Fig. 4, a linear fitting is conducted for the results obtained by MD simulations. The thermal conductivity of the BP/GE bilayer heterostructures along the zigzag and the armchair directions is 206.61 ± 6.35 and 51.02 ± 3.72 W m $^{-1}$ K $^{-1}$, respectively. Our results show that the in-plane thermal conductivity of the infinite-size BP/GE bilayer heterostructures exhibits a stronger anisotropy ratio of approximately 4.0 compared to single-layer BP. The stronger anisotropy may be attributed to the interaction between BP and GE in the bilayer

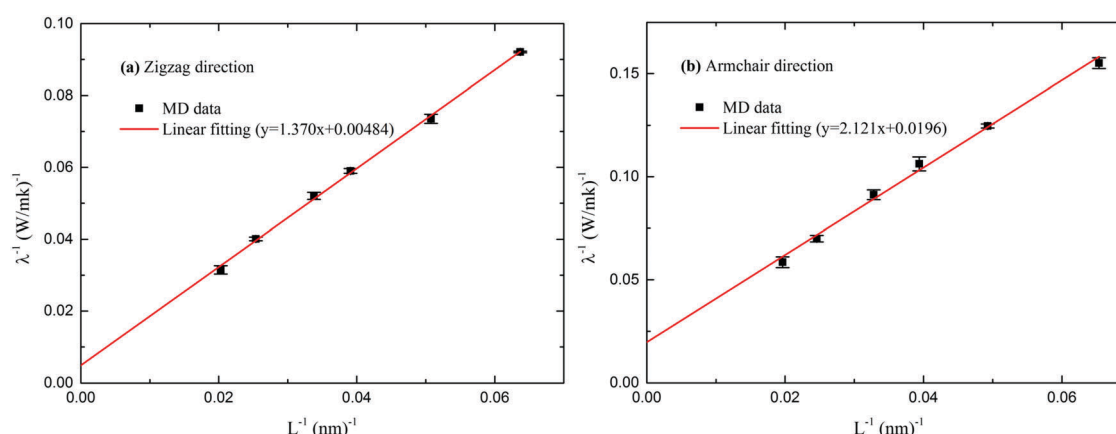


Fig. 4 Inverse thermal conductivity $1/k$ as a function of the inverse simulation BP/GE length $1/L$ in NEMD simulations: (a) along the zigzag direction and (b) armchair direction. The thermal conductivity at infinitely large BP/GE heterostructures can be obtained by linear extrapolation at $1/L = 0$.

heterostructures that strengthens the BP puckered configuration in the armchair direction, which has been demonstrated to be the cause of anisotropy in single-layer BP.^{43–45}

3.1.2 Effect of the interface coupling strength. In previous studies,^{16,18} the interface thermal conductance of two-dimensional material heterostructures was effectively adjusted by changing the coupling strength. However, it is confusing whether the coupling strength has the same effect on the in-plane thermal conductivity of the heterostructures. In the simulation, we regulate the strength of interaction of the non-bonded van der Waals force between BP and GE by adjusting the parameter χ (see eqn (1)). To check the effect of the interlayer interaction strength on in-plane thermal conductivity, we change the scaling factor χ from 1 to 6, with the results shown in Fig. 5. It is found that the BP/GE thermal conductivity along the zigzag direction increases as χ increases up to 4 and then decreases, while the BP/GE thermal conductivity along the armchair direction increases as χ increases up to $\chi = 5$ and then decreases. Here, instead of putting emphasis on the absolute values of thermal conductivity, we focus on the effect of coupling strength on the thermal transport of the BP/GE heterostructures; thus, we do not consider the size effect in the following research.

The increase in BP/GE thermal conductivity with the interface coupling strength χ can be explained from two aspects: (1) when the interface coupling strength increases, the phonon coupling between BP and GE is enhanced, which directly increases the efficiency of the in-plane thermal transport. (2) Group velocities of the out-of-plane and in-plane phonons in the BP of the heterostructures are strengthened, which leads directly to an increase in the thermal conductivity of BP, thereby indirectly increasing the thermal conductivity of BP/GE.

The PDOS is investigated to obtain an in-depth understanding of the heat transfer mechanisms in the BP/GE heterostructures. Fig. 6 and 7 show that the out-of-plane phonon spectra of BP and GE along the zigzag direction make a greater contribution compared to the in-plane phonon spectra. Meanwhile, both the in-plane and out-of-plane overlap factors S , which are calculated using eqn (7), increase with increasing

coupling strength, and the overlapping vibration spectra, mainly in the low frequency zone, range from 1 to 15 THz.⁴⁶ The regularity with which this occurs suggests that the main channel for heat transport in the BP/GE heterostructures is the coupling between the low-frequency out-of-plane phonons. From Fig. 6, the out-of-plane overlap factor S increases from 0.2996 to 0.3280 when the coupling strength ranges from 1 to 4. The same trend appears in the BP/GE heterostructures along the armchair direction, as shown in Fig. 7, which is in agreement with the BP/GE thermal conductivity along the armchair direction increasing as χ increases up to $\chi = 5$, with the overlap factor S increasing from 0.3100 to 0.3162. This is because a higher interlayer interaction strength leads to a better match for the PDOS curves of BP and GE, facilitating heat transport in the BP/GE heterostructures so that heat can be exchanged easily at the interface between BP and GE, and the emergence of a higher value for S .

However, the in-plane thermal conductivity of BP/GE along the zigzag direction decreases when the coupling strength is 5, while the thermal conductivity of BP/GE along the armchair direction decreases when the coupling strength is 6. The overlap factor S for both in-plane and out-of-plane components along the zigzag direction and armchair direction almost keep the trend of increasing, which is not consistent with the change trend for the thermal conductivity of BP/GE. This thermal conductivity decrease induced by the coupling strength is quite surprising, since it is well known that strong coupling strength enhances the thermal conductivity of crystal materials. To study the thermal conductivity of BP in BP/GE and further understand the decrease in BP/GE thermal conductivity at a coupling strength of 5 (along the zigzag direction) and 6 (along the armchair direction), we calculated the thermal conductivity of BP in the BP/GE heterostructures in the next section.

3.2 In-plane thermal conductivity of black phosphorene in the BP/GE heterostructures

3.2.1 Effect of the interface coupling strength. Improving the thermal conductivity of BP is very important for promoting

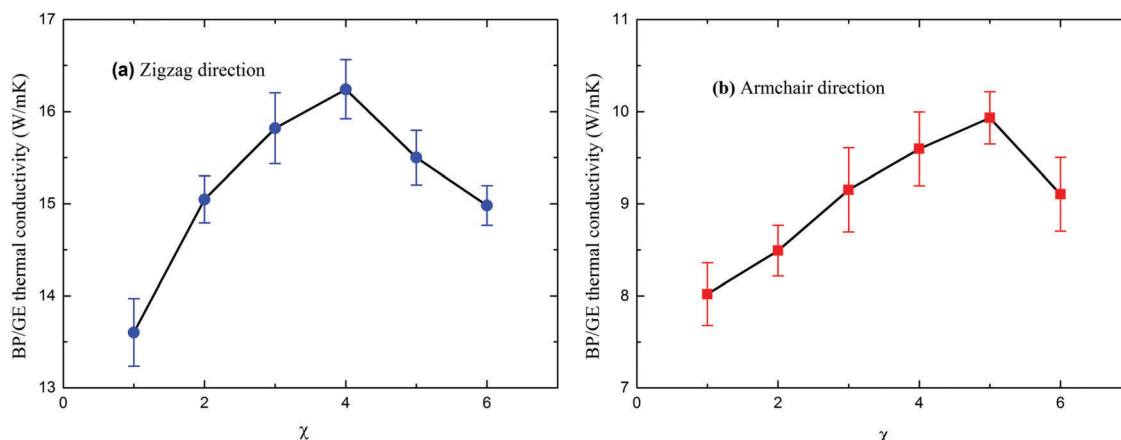


Fig. 5 Dependence of BP/GE thermal conductivity (a) along the zigzag direction and (b) armchair direction for different values of the interlayer interaction strength χ .

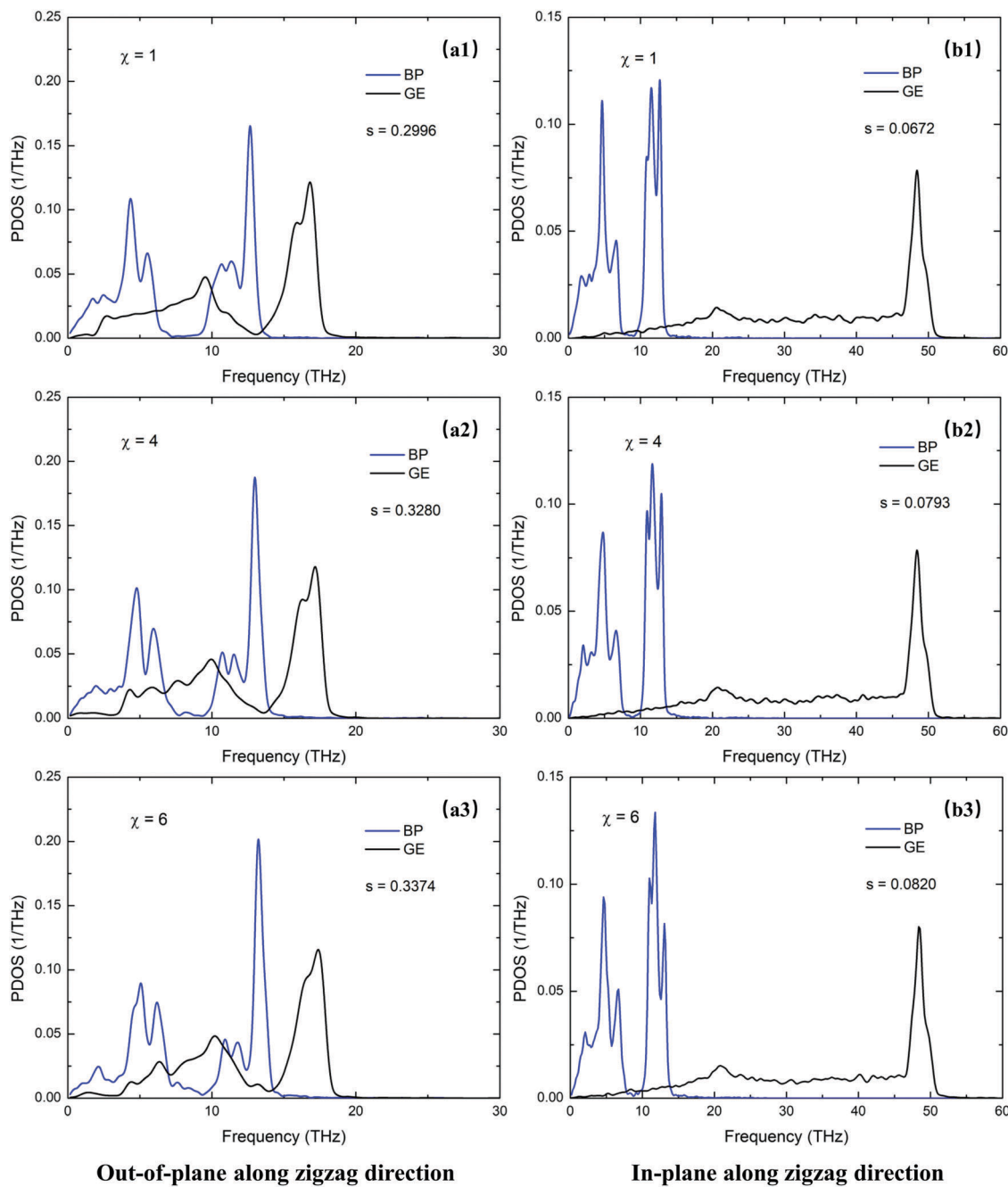


Fig. 6 Out-of-plane and in-plane PDOS of BP and GE atoms at different interface coupling strengths along the zigzag direction.

its application in nanodevices. Recent studies^{15,45} have revealed that the thermal conductivity of BP can be improved by different methods such as changing the coupling strength of the substrate. It has been well-known that the coupling strength can significantly impact the thermal transport properties.

To study the effect of the coupling strength on the thermal conductivity of BP in heterostructures, different powers Q are used to stabilize the structure and applied in the length direction to calculate the corresponding thermal conductivity. Fig. 8(a and b) shows the effect of coupling strength on the thermal conductivity of BP in the BP/GE heterostructures along

both the zigzag and armchair directions. From Fig. 8(a and b), the thermal conductivity of BP in the BP/GE heterostructures along the zigzag direction increases linearly as χ increases up to 4 and then decreases, while the BP/GE thermal conductivity along the armchair direction increases almost linearly as χ increases up to 5 and then decreases. It is obvious that the trend is consistent with the variation of the BP/GE thermal conductivity in Fig. 5, which indicates that the variation of the BP/GE thermal conductivity is largely due to the thermal conductivity of BP in the BP/GE heterostructures varying with the degree of coupling of the phonons. Moreover, we calculated

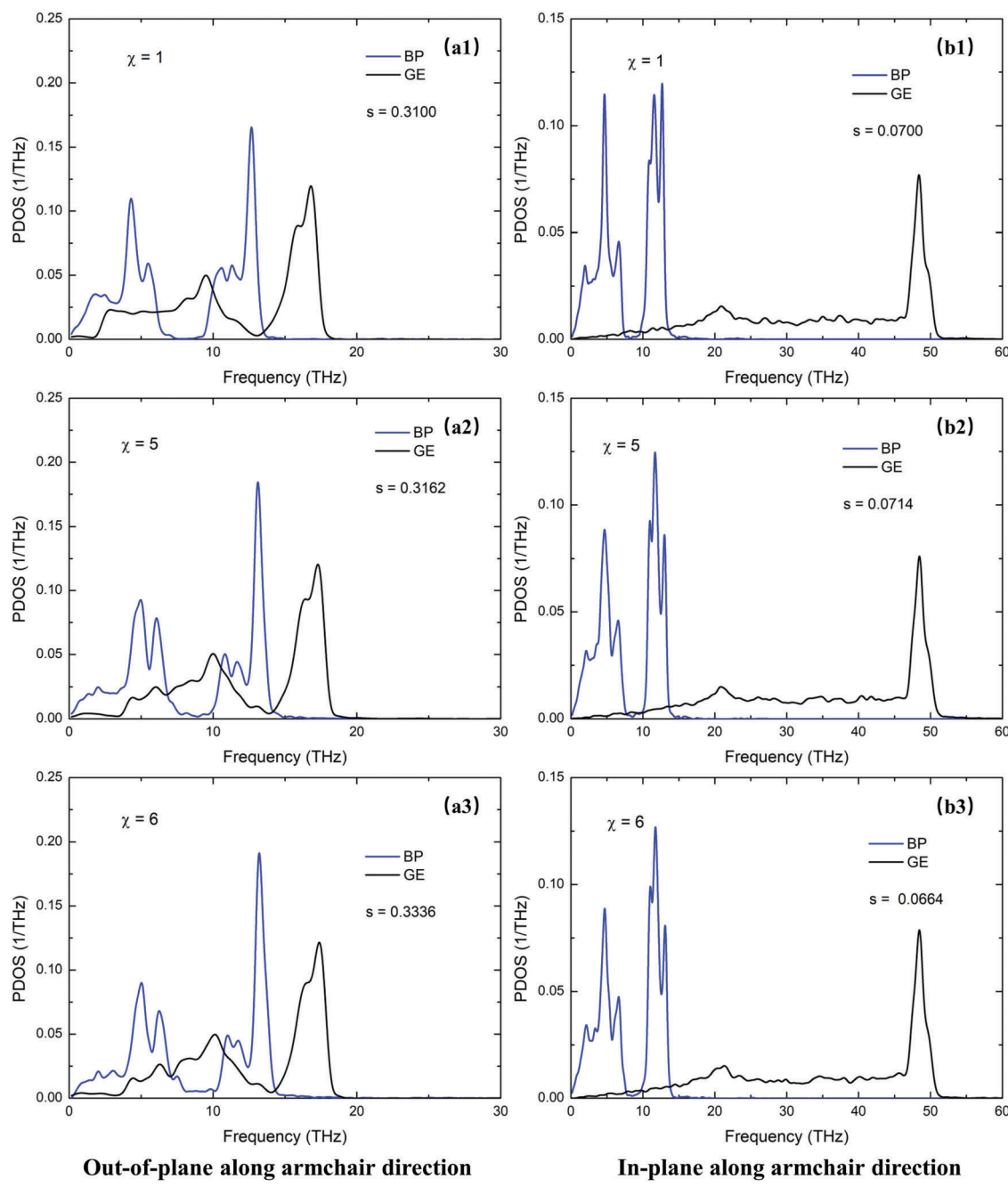


Fig. 7 Out-of-plane and in-plane PDOS of BP and GE atoms at different interface coupling strengths along the armchair direction.

the thermal conductivity of GE in the BP/GE heterostructures and found that it gradually decreased as the coupling strength increased, as schematically shown in Fig. 8(c). This is because the interlayer vdW interactions between BP and GE increase with increasing coupling strength, which restricts the flexural mode of GE, resulting in a decrease in the thermal conductivity of graphene.^{47–49} Therefore, the deflection behavior of the dependence of the in-plane thermal conductivity of BP/GE on the coupling strength can be explained as follows: When χ is small, the increase in the thermal conductivity of BP in BP/GE is dominant; when χ is large, the thermal conductivities of BP

and GE both decrease, thus resulting in the observed non-monotonic dependence of thermal conductivity on χ , as shown in Fig. 5.

PDOS analyses are also performed to further understand the non-monotonic trend for the thermal conductivity of BP in BP/GE. Fig. 9 and 10 show that the peaks for the out-of-plane PDOS of BP along the zigzag and armchair directions both exhibit a blue shift, such as from 12.73 THz at $\chi = 1$ to 13.20 THz at $\chi = 6$ along the zigzag direction and from 12.56 THz at $\chi = 1$ to 13.08 THz at $\chi = 6$ along the armchair direction. The blue shift of the peaks also appears in the PDOS

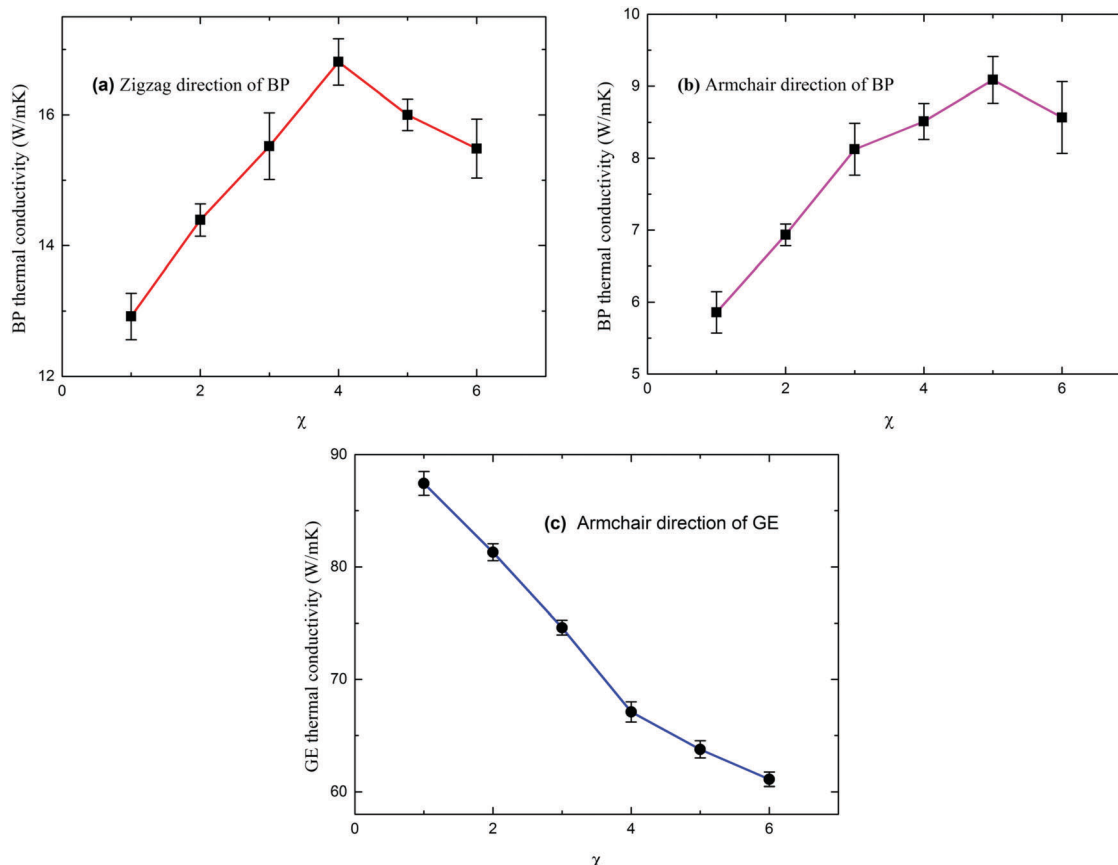


Fig. 8 Dependence of BP and GE thermal conductivity in BP/GE heterostructures (a) BP along the zigzag direction, (b) BP along the armchair direction and (c) GE along the armchair direction for different values of the interlayer interaction strength χ . We only calculated the thermal conductivity of GE along the armchair direction, due to its in-plane isotropy.

for the in-plane along the zigzag and armchair directions. Therefore, the enhancement of the coupling strength results in stiffening of the phonons transferring in BP, which increases the phonon group velocities and results in an enhanced thermal conductivity according to the classical lattice thermal transport theory.⁵⁰ The phonon coupling strength is enhanced at both in-plane and out-of-plane components, and the corresponding

BP thermal conductivity in the BP/GE heterostructures along the zigzag (at $\chi = 1\text{--}4$) and armchair (at $\chi = 1\text{--}5$) directions increases at different coupling strengths with the same tendency. For the observed decrease in the BP thermal conductivity at a coupling strength of 5 (along the zigzag direction) and 6 (along the armchair direction), the following explanation may be the cause of the results. When the coupling strength

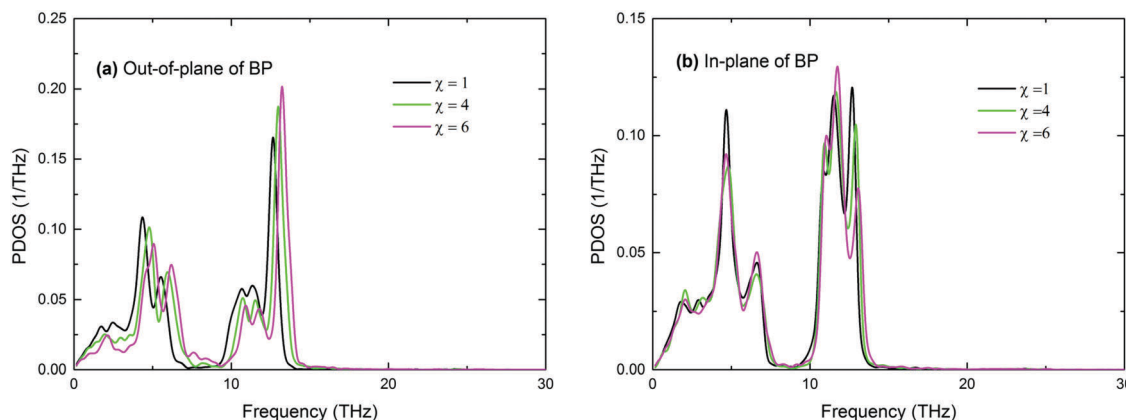


Fig. 9 PDOS of BP in BP/GE heterostructures at different interface coupling strengths along the zigzag direction. (a) Out-of-plane PDOS of BP and (b) in-plane PDOS of BP.

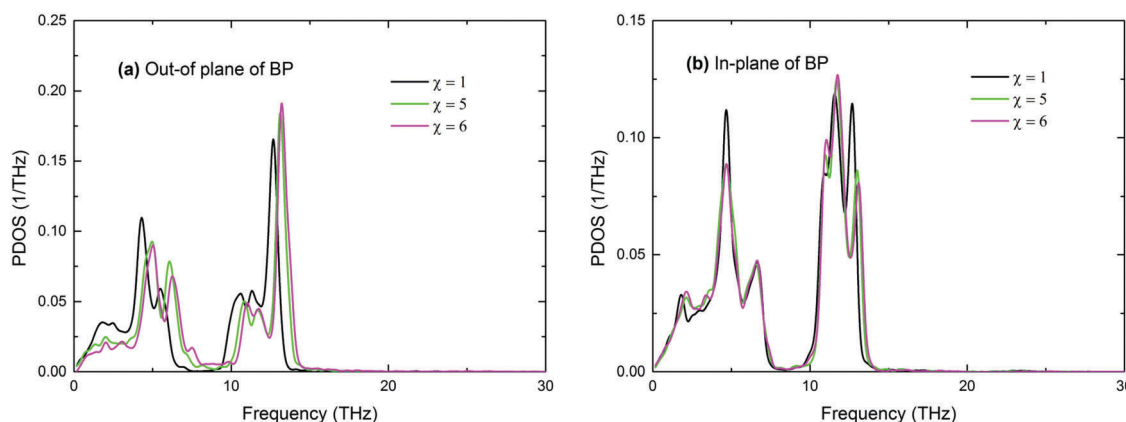


Fig. 10 PDOS of BP in BP/GE heterostructures at different interface coupling strengths along the armchair direction. (a) Out-of-plane PDOS of BP and (b) in-plane PDOS of BP.

increased to a certain extent, the interaction between BP and GE became stronger; thus, the flexural mode in BP⁴⁵ and GE,^{48,49} which is caused by the motion perpendicular to the two dimensional plane, was restricted, and the thermal conductivity of BP decreased with the coupling strength. At this point, we can conclude that the decrease of the BP/GE thermal conductivity is due to the strong coupling strength that restricts the flexural modes of BP and GE.

3.2.2 Effect of hydrogenation. In recent years, the chemical functionalization of GE has attracted much attention and has been used to modify its physical, chemical and mechanical properties.^{51–53} Similarly, hydrogenated GE is used to regulate the thermal conductivity of heterostructures and has been demonstrated to be an effective way to improve the interface thermal conductance.^{17,54} In this work, the effects of hydrogenation on BP thermal conductivity in the BP/GE heterostructures are studied. To keep the initial structure reasonable, the interaction strength value χ is set as 1 in the following calculations, with a C-H bond length of 1.14. The hydrogen coverage is defined as $f = N/M$, where M denotes half the number of total C atoms in GE, and N denotes the number of

H atoms on one side, which is the middle position of bilayer heterostructures in our research, as schematically shown in Fig. 1(d). Since a higher hydrogen coverage ($>10\%$) on one side of GE leads to a distorted graphene structure, we only consider the effect of a low hydrogenation rate ($<6\%$) on the thermal conductivity of BP.

Fig. 11 shows the dependence of the BP thermal conductivity in the BP/GE heterostructures (a) along the zigzag direction and (b) armchair direction for varying hydrogen coverage. From Fig. 11 (a), we observe that the BP thermal conductivity along the zigzag direction increases monotonically with f . When the hydrogen coverage is 5%, the thermal conductivity of BP in the BP/GE heterostructures along the zigzag direction is $15.42 \pm 0.37 \text{ W m}^{-1} \text{ K}^{-1}$, which is 19.3% higher than that of pristine BP in the BP/GE heterostructures, indicating that hydrogenation effectively enhances the in-plane thermal conductivity of BP. From Fig. 11 (b), when the hydrogen coverage is 1%, the BP thermal conductivity in the BP/GE heterostructures along the zigzag direction increases obviously, and when the hydrogen coverage is 2–5%, its thermal conductivity increases slowly. The possible reasons for the increase in the thermal

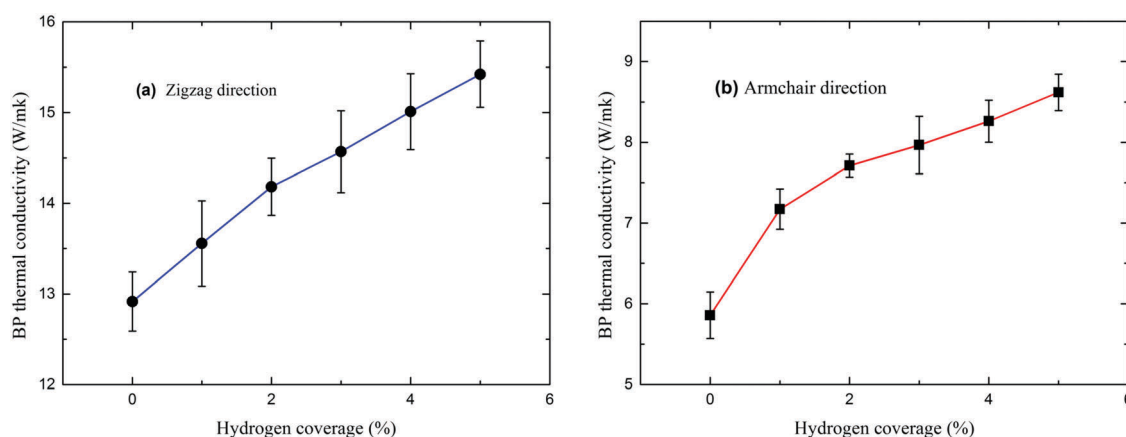


Fig. 11 Dependence of BP thermal conductivity in BP/GE heterostructures (a) along the zigzag direction and (b) armchair direction for varying hydrogen coverage (<6%).

conductivity of BP along the zigzag and armchair directions are as follows: with the existence of hydrogen atoms, a new channel is opened for out-of-plane phonon coupling between BP and GE, which greatly enhances the thermal transport across the interfaces, and indirectly improves the phonon coupling in BP.

To gain further insight into the degree of phonon couplings, a detailed analysis of the PDOS under varying H coverage is conducted for both the zigzag and armchair directions, as shown in Fig. 12. As mentioned above, there is mainly an out-of-plane phonon coupling between BP and GE, so here, we only discuss the out-of-plane phonon coupling. Fig. 12 shows

the out-of-plane phonon PDOS along both the zigzag and armchair directions at 1%, 3%, and 5% hydrogen coverage. As the hydrogenation ratio increases, the out-of-plane overlap S between BP and GE increases. The improvement in the out-of-plane phonon couplings along both the zigzag and armchair directions indirectly facilitates the thermal transport in BP and GE. In the meantime, stronger phonon coupling between BP and GE in the out-of-plane along both the zigzag and armchair directions provides a more convenient channel for the phonon coupling in BP. Therefore, with stronger phonon coupling caused by the introduction of hydrogen atoms, the thermal

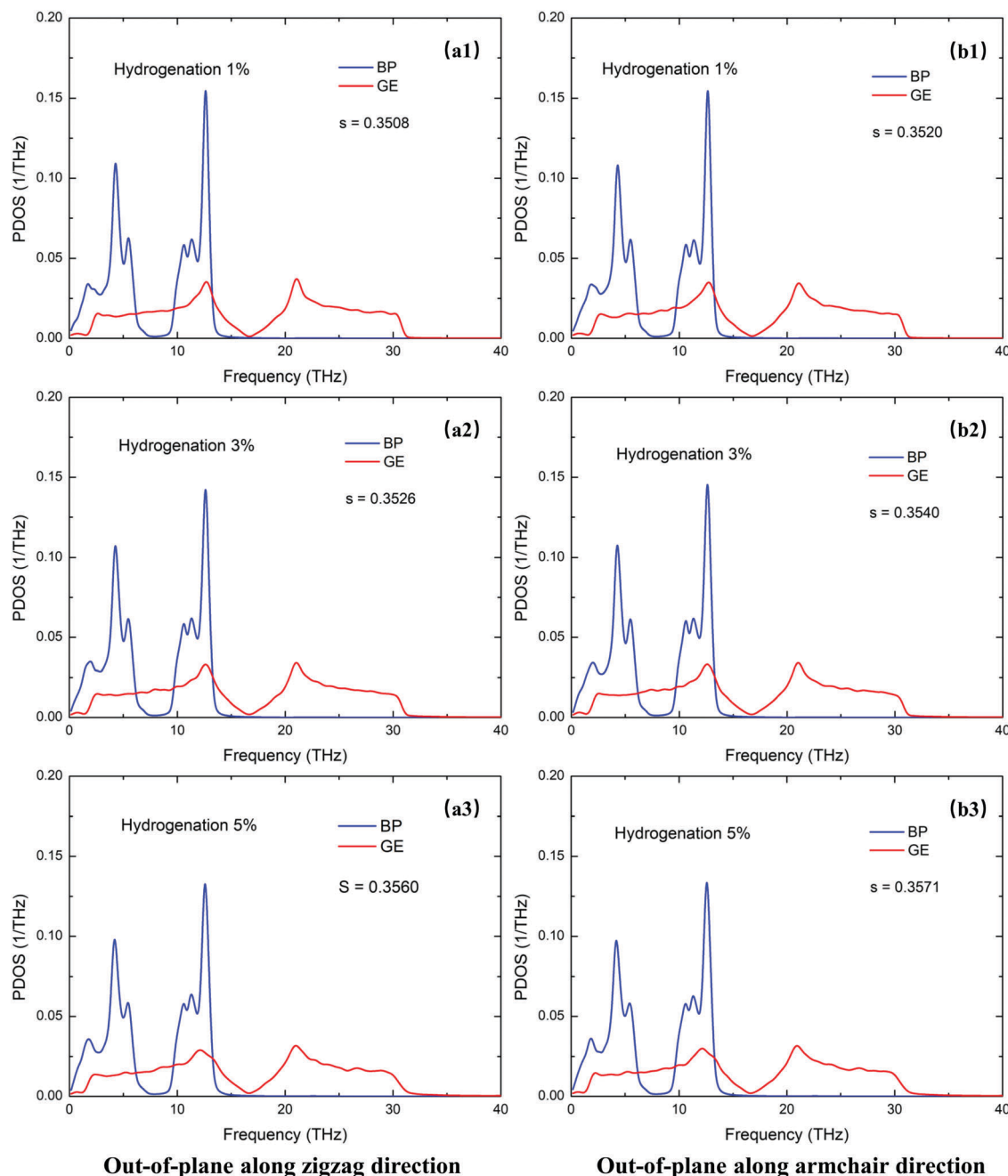


Fig. 12 Out-of-plane PDOS of BP and GE atoms at varying hydrogen coverage (a1–a3) along the zigzag and (b1–b3) armchair directions.

conductivity of BP in the BP/GE heterostructures increases with increasing hydrogen coverage.

4. Conclusion

The in-plane thermal transport in BP/GE bilayer heterostructures is studied using MD simulations. The in-plane thermal conductivity of bilayer structure heterostructures and BP in heterostructures is calculated. The effect on in-plane thermal conductivity with respect to sample length, coupling strength, and hydrogen coverage is systematically examined. From the simulation results, it is found that the in-plane thermal conductivity of infinite-size BP/GE bilayer heterostructures exhibits a stronger anisotropy ratio of 4.0 compared to single-layer BP. This may be due to the fact that a heterogeneous structure strengthens its puckered configuration in the armchair direction. We found that the thermal conductivity of the BP/GE heterostructures or BP in heterostructures shows the same trend when the coupling strength is enhanced. This can be explained by the PDOS, which indicates that the variation in the BP/GE thermal conductivity is largely due to the thermal conductivity of BP in the BP/GE heterostructures varying with the degree of coupling of the phonons. Moreover, we calculated the thermal conductivity of GE in the BP/GE heterostructures and found that the decrease in BP/GE thermal conductivity is due to the strong coupling strength, which restricts the flexural modes of BP and GE. In addition, we found that hydrogenation can effectively enhance the thermal conductivity of BP in heterostructures due to an indirect increase in the phonon coupling strength of BP following the addition of hydrogen atoms. This study is of significance for understanding the thermal transport behavior of the BP/GE heterostructures and BP in heterostructures and promoting their future applications in thermal management and thermoelectric devices.

Conflicts of interest

There are no conflicts to declare.

Acknowledgements

The author(s) disclosed receipt of the following financial support for the research, authorship, and/or publication of this article: the authors acknowledge the financial support provided by the National Natural Science Foundation of China (Project no. 51506033), the Innovation Project of Guet Graduate Education (Grant no. 2018YJCX03), the Guangxi Natural Science Foundation (Grant no. 2017JJA160108), and the GUET Excellent Graduate Thesis Program (Grant no. 16YJPYSS03).

References

- C. Lee, X. Wei, J. W. Kysar and J. Hone, *Science*, 2008, **321**, 385–388.
- M. Q. Chen, S. S. Quek, Z. D. Sha, C. H. Chiu, Q. X. Pei and Y. W. Zhang, *Carbon*, 2015, **85**, 135–146.
- C. Soldano, A. Mahmood and E. Dujardin, *Carbon*, 2010, **48**, 2127–2150.
- A. A. Balandin, S. Ghosh, W. Bao, I. Calizo, D. Teweldebrhan, F. Miao and C. N. Lau, *Nano Lett.*, 2008, **8**, 902.
- J. Chen, G. Zhang and B. Li, *Nanoscale*, 2013, **5**, 532–536.
- Y. Cai, G. Zhang and Y. W. Zhang, *J. Am. Chem. Soc.*, 2014, **136**, 6269.
- T. Georgiou, R. Jalil, B. D. Belle, L. Britnell, R. V. Gorbachev, S. V. Morozov, Y. J. Kim, A. Gholinia, S. J. Haigh and O. Makarovsky, *Nat. Nanotechnol.*, 2013, **8**, 100.
- A. K. Geim and I. V. Grigorieva, *Nature*, 2013, **499**, 419–425.
- M. Modarresi, M. R. Roknabadi and N. Shahtahmassebi, *Phys. B*, 2013, **415**, 62–66.
- J. Liang, H. Bi, D. Wan and F. Huang, *Adv. Funct. Mater.*, 2012, **22**, 1267–1271.
- S. Kim, T. H. Seo, M. J. Kim, K. M. Song, E. Suh and H. Kim, *Nano Res.*, 2015, **8**, 1327–1338.
- A. Ebnonnasir, B. Narayanan, S. Kodambaka and C. V. Ciobanu, *Appl. Phys. Lett.*, 2014, **105**, 31603.
- J. Zhu, J. Zhang and Y. Hao, *Jpn. J. Appl. Phys.*, 2016, **55**, 80306.
- W. Hu, T. Wang and J. Yang, *J. Mater. Chem. C*, 2015, **3**, 4756–4761.
- Q. X. Pei, X. Zhang, Z. Ding, Y. Y. Zhang and Y. W. Zhang, *Phys. Chem. Chem. Phys.*, 2017, **19**, 17180–17186.
- B. Liu, J. A. Baimova, C. D. Reddy, A. W. Law, S. V. Dmitriev, H. Wu and K. Zhou, *ACS Appl. Mater. Interfaces*, 2014, **6**, 18180–18188.
- Z. Ding, Q. X. Pei, J. W. Jiang, W. Huang and Y. W. Zhang, *Carbon*, 2016, **96**, 888–896.
- B. Liu, F. Meng, C. D. Reddy, J. A. Baimova, N. Srikanth, S. V. Dmitriev and K. Zhou, *RSC Adv.*, 2015, **5**, 29193–29200.
- Y. Cai, G. Zhang and Y. W. Zhang, *J. Phys. Chem. C*, 2015, **119**, 13929–13936.
- P. Chen, N. Li, X. Chen, W. J. Ong and X. Zhao, *2D Mater.*, 2017, **5**, 14002.
- L. Li, Y. Yu, G. J. Ye, Q. Ge, X. Ou, H. Wu, D. Feng, X. H. Chen and Y. Zhang, *Nat. Nanotechnol.*, 2014, **9**, 372–377.
- G. Qin, Q. B. Yan, Z. Qin, S. Y. Yue, M. Hu and G. Su, *Phys. Chem. Chem. Phys.*, 2014, **17**, 4854–4858.
- Z. Xu and M. J. Buehler, *J. Phys.: Condens. Matter*, 2012, **24**, 475305.
- K. F. Mak, C. H. Lui and T. F. Heinz, *Appl. Phys. Lett.*, 2010, **97**, 109.
- J. E. Padilha, A. Fazzio and A. J. R. Da Silva, *Phys. Rev. Lett.*, 2015, **114**, 66803.
- X. Zhang, S. Yue, Z. Qin, H. Wang, Y. Han, M. Hu and G. Qin, *Phys. Rev. B*, 2016, **94**, 165445.
- Z. Jie, P. Haechan, C. J. Yang, G. Xiaokun, Z. Hu, K. Sreejith, W. Nathaniel, S. A. Campbell, D. Matthew, D. Xu, L. Mo, W. J. Ping, Y. Ronggui and W. Xiaoja, *Adv. Electron. Mater.*, 2016, **2**, 1600040.
- K. Saito, J. Nakamura and A. Natori, *Phys. Rev. B: Condens. Matter Mater. Phys.*, 2007, **76**, 3398–3407.
- S. Plimpton, *J. Comput. Phys.*, 1995, **117**, 1–19.

- 30 D. W. Brenner, O. A. Shenderova, J. Harrison, S. J. Stuart, B. Ni and S. B. Sinnott, *J. Phys.: Condens. Matter*, 2002, **14**, 783–802.
- 31 J. W. Jiang, *Nanotechnology*, 2015, **26**, 315706.
- 32 A. K. Rappe, C. J. Casewit, K. S. Colwell, W. A. G. Iii and W. M. Skiff, *J. Am. Chem. Soc.*, 1992, **114**, 10024–10035.
- 33 W. C. Swope, H. C. Andersen, P. H. Berens and K. R. Wilson, *J. Chem. Phys.*, 1982, **76**, 637–649.
- 34 P. Jund and R. Jullien, *Phys. Rev. B: Condens. Matter Mater. Phys.*, 1999, **59**, 13707–13711.
- 35 J. M. Dickey and A. Paskin, *Phys. Rev. B: Condens. Matter Mater. Phys.*, 1969, **188**, 1407–1418.
- 36 Q. X. Pei, Y. W. Zhang, Z. D. Sha and V. B. Shenoy, *Appl. Phys. Lett.*, 2012, **100**, 90.
- 37 Q. X. Pei, Z. D. Sha and Y. W. Zhang, *Carbon*, 2011, **49**, 4752–4759.
- 38 J. Tersoff, *Phys. Rev. B: Condens. Matter Mater. Phys.*, 1989, **39**, 5566–5568.
- 39 L. Lindsay and D. A. Broido, *Phys. Rev. B: Condens. Matter Mater. Phys.*, 2010, **81**, 262–265.
- 40 B. Li, L. Huang, M. Zhong, Y. Li, Y. Wang, J. Li and Z. Wei, *Adv. Electron. Mater.*, 2016, **2**, 1600298.
- 41 P. K. Sahoo, S. Memaran, Y. Xin, L. Balicas and H. R. Gutiérrez, *Nature*, 2018, **553**, 63–67.
- 42 S. R. Phillpot, P. Kebbinski and P. K. Schelling, *Phys. Rev. B: Condens. Matter Mater. Phys.*, 2002, **65**, 144306.
- 43 Z. Y. Ong, Y. Cai, G. Zhang and Y. W. Zhang, *J. Phys. Chem. C*, 2014, **118**, 25272–25277.
- 44 L. Kou, C. Chen and S. C. Smith, *J. Phys. Chem. Lett.*, 2015, **6**, 2794.
- 45 J. Chen, S. Chen and Y. Gao, *J. Phys. Chem. Lett.*, 2016, **7**, 2518.
- 46 D. A. Broido, N. Mingo and L. Lindsay, *Phys. Rev. B: Condens. Matter Mater. Phys.*, 2010, **82**, 115427.
- 47 S. Ghosh, W. Bao, D. L. Nika, S. Subrina, E. P. Pokatilov, C. N. Lau and A. A. Balandin, *Nat. Mater.*, 2010, **9**, 555.
- 48 L. Lindsay, D. A. Broido and N. Mingo, *Phys. Rev. B: Condens. Matter Mater. Phys.*, 2011, **83**, 1417–1425.
- 49 Z. Wei, Z. Ni, K. Bi, M. Chen and Y. Chen, *Carbon*, 2011, **49**, 2653–2658.
- 50 L. Shi, *Nanoscale Microscale Thermophys. Eng.*, 2012, **16**, 79–116.
- 51 T. Kuila, S. Bose, A. K. Mishra, P. Khanra, N. H. Kim and J. H. Lee, *Prog. Mater. Sci.*, 2012, **57**, 1061–1105.
- 52 D. W. Boukhvalov and M. I. Katsnelson, *Nano Lett.*, 2008, **8**, 4373–4379.
- 53 A. K. Singh and B. I. Yakobson, *Nano Lett.*, 2009, **9**, 1540.
- 54 J. Zhang, Y. Hong and Y. Yue, *J. Appl. Phys.*, 2015, **117**, 3917–3921.